European Journal of Mechanics / A Solids 73 (2019) 500–511

Contents lists available at ScienceDirect

European Journal of Mechanics / A Solids

journal homepage: www.elsevier.com/locate/ejmsol

A dual interpolation boundary face method for elasticity problems

Jianming Zhang*, Weicheng Lin, Yunqiao Dong

State Key Laboratory of Advanced Design and Manufacturing for Vehicle Body, College of Mechanical and Vehicle Engineering, Hunan University, Changsha, 410082, China

ARTICLE INFO

Keywords:
Dual interpolation boundary face method
Boundary element method
Moving least-squares approximation

ABSTRACT

A dual interpolation boundary face method (DiBFM) is proposed to unify the conforming and nonconforming elements in boundary element method (BEM) implementation. In the DiBFM, the nodes of a conventional conforming element are sorted into two groups: the nodes on the boundary (called virtual nodes) and the internal nodes (called source nodes). Without virtual nodes, the conforming element turns to be a conventional nonconforming element of a lower order. Physical variables are interpolated using the conforming elements, the same way as conforming BEM. Boundary integral equations are collocated at source nodes, the same way as nonconforming BEM. To make the final system of linear equations solvable, additional constraint equations are required to condense the degrees of freedom for all the virtual nodes. These constraints are constructed using the moving least-squares (MLS). Besides, both boundary integration and MLS are performed in the parametric spaces of curves, namely, the geometric data, such as coordinates, out normals and Jacobians, are calculated directly from curves rather than from elements. Thus, no geometric errors are introduced no matter how coarse the discretization is. The method has been implemented successfully for solving two-dimensional elasticity problems. A number of numerical examples with real engineering background have demonstrated the accuracy and efficiency of the new method.

1. Introduction

The boundary element method (BEM) is a popular numerical technique for solving engineering problems. It has been widely applied to solve potential problems (Zhang et al., 2009, 2017a; Ang and Yun, 2011; Gao et al., 2017), elastostatic problems (Schnack and Chen, 2001; Zhang et al., 2011, 2018; Sladek and Sladek, 1992; Wang and Qin, 2012), elastodynamic problems (Tanaka and Chen, 2001; Li et al., 2014; Zhao et al., 2015), contact problems (Blázquez and París, 2011; Shu et al., 2016; Rodríguez-Tembleque et al., 2011), fracture mechanics problems (Xie et al., 2014; Wünsche et al., 2012; Dong et al., 2011; Lei et al., 2015) and acoustics problems (Peake et al., 2015; Shen and Liu, 2007; Chen et al., 2010; Wang et al., 2013). This is mainly due to its unique advantages in higher accuracy, dimension reduction and naturally treating infinite domain problems without the need for artificial boundary conditions or domain truncation. The method is also popular because it can use the nonconforming elements, which is the most important advantage of BEM (Citarella et al., 2018; Carlone et al., 2016). This makes the mesh generation a simpler process than with conforming elements like the finite element method (FEM). However, how to take full advantages of this feature has been a long-standing issue in the BEM community, because the conforming and nonconforming elements each have their own advantages and disadvantages (Floreza and Powera, 2001; Manolis and Banerjee, 1986; Parreira, 1988).

Use of conforming elements (see Fig. 1 (a)) leads to certain difficulties at geometric corners and physical corners (e.g., points which boundary condition is discontinuous). At geometric corners, the traction in elasticity problem and the normal flux in potential problem are ill-defined because of the ambiguity in the direction of the normal. At physical corners, the approximation of the discontinuous field is very inaccurate, because the shape functions of conforming elements maintain the continuity of the fields. A way of avoiding these difficulties is by using multiple-node method (Mitra and Ingber, 1993). In this method, multiple source nodes are placed at corners (see Fig. 1 (b)). These nodes, however, can lead to a set of linearly dependent equations, if Dirichlet boundary conditions are specified on the two adjacent edges. Obviously, the final system of equations cannot be solvable. Besides, the multiple-node method and conforming element method cannot guarantee the $C^{1,\alpha}$ continuity, which is necessary for hypersingular integral (Guiggiani et al., 1992).

Use of nonconforming elements (see Fig. 1 (c)) is able to naturally overcome these difficulties. The nonconforming element has some attractive advantages, such as simplifying the treatment of corner

* Corresponding author.
E-mail address: zhangjm@hnu.edu.cn (J. Zhang).

https://doi.org/10.1016/j.euromechsol.2018.10.011
Received 26 March 2018; Received in revised form 24 September 2018; Accepted 15 October 2018
Available online 19 October 2018
0997-7538/

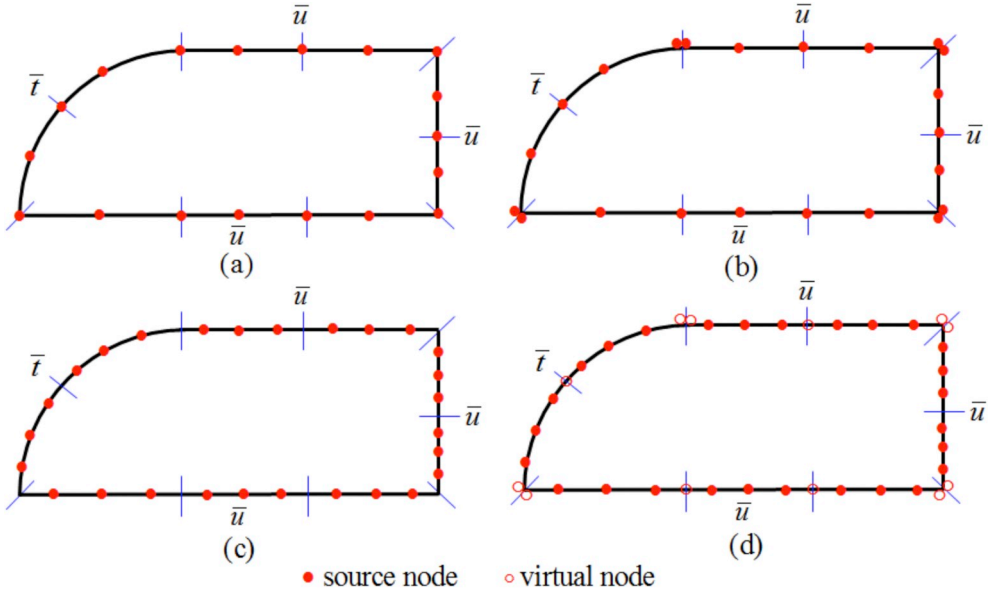

Fig. 1. Boundary discretized by quadratic elements: (a) conforming elements, (b) conforming elements with multiple-node method, (c) nonconforming elements, and (d) dual interpolation elements.

problems, the evaluation of the hypersingular integral and the mesh generation. Since the source nodes of the nonconforming element are inside the element, the field variables at the interfaces between elements must be interpolated from values at the interior nodes. Thus, some inaccuracies are introduced. For the same level of accuracy, nonconforming element requires much more source nodes than conforming element. This means more computer resources and CPU time.

To cope with the problems above, we have developed the double-layer interpolation method (Zhang et al., 2017b), here called dual interpolation method. A primary goal of our research is to unify the conforming and nonconforming elements in BEM implementation. Another goal is to improve the performance of the BEM. Yet another goal is to simplify the mesh generation. The dual interpolation method is obtained by coupling the conventional polynomial element interpolation with the moving least-squares (MLS) approximation. The nodes of a dual interpolation element are sorted into two groups: virtual and source nodes (see Fig. 1(d)). With virtual and source nodes, it is equivalent to a standard conforming element. Without virtual nodes, it turns to be a conventional nonconforming element of a lower order. Besides, it has the following features: (i) improving the interpolation accuracy of the original nonconforming element by two orders; (ii) accurately approximating both continuous and discontinuous fields by manipulating the influence domains of some specific virtual nodes in the MLS; and (iii) simplifying the treatment of corner problems and the evaluation of the hypersingular integral, because the boundary integral equation (BIE) is collocated at source nodes rather than virtual nodes.

In this paper, the dual interpolation method is combined with the boundary face method (BFM) (Zhang et al., 2009; Shu et al., 2016; Wang et al., 2013) to solve the 2D elasticity problems at first time. We call the combined method the dual interpolation boundary face method (DiBFM). In the new method, displacements and tractions are interpolated using dual interpolation elements (first-layer interpolation), the same way as conforming BEM. BIEs are collocated at source nodes, only, the same way as nonconforming BEM. In consequence, the number of linear equations obtained by discretizing the BIE is less than the number of unknown nodal values. To make the final system of linear equations solvable, additional constraint equations must be needed to condense the degrees of freedom for all virtual nodes. These equations are constructed by the MLS approximation (second-layer interpolation). For the same number of source nodes, the size of the final coefficient matrix in the DiBFM is the same as that in the conventional BEM, while the DiBFM is able to possess higher computational accuracy. This is a major advantage of our method.

In the DiBFM implementation, both boundary integration and dual interpolation are performed in the parametric spaces of each curve, which are exactly same as the boundary representation (B-rep) data structure. As the B-rep data structure is used in most CAD software, it has the potential to seamlessly interact with CAD software. The geometric errors can be avoided even in a coarse grid, because the geometric data are calculated directly from the curves rather than from dual interpolation elements. In addition, the MLS in the DiBFM is just used to assemble the coefficient matrices, rather than evaluate the shape functions at each Gaussian point in boundary integration. Meanwhile, in the process of MLS computation, the source nodes covered in the influence domain of a virtual node are obtained by directly searching the neighboring three layer elements, instead of looping over all source nodes located on the curve. Thus, the efficiency of the MLS in a pure mesh-free method is lower than that of MLS in the DiBFM.

The extensions of the DiBFM to solve three-dimensional (3D) problems will substantially simplify the mesh generation. This is an attractive advantage of our method. The reasons for this include the following: (i) discontinuous grids are much easier to generate than continuous grids (see Fig. 2); and (ii) both continuous and discontinuous fields can be naturally and accurately approximated by dual interpolation method, even if discontinuous grids are used.

This paper is organized as follows. In Section 2, the parameter mapping scheme for 2D problems is briefly described. Section 3 describes the dual interpolation method for elasticity problem. A general formulation of the DiBFM for elasticity problem is described in Section 4. A number of numerical examples are given in Section 5. The paper ends with conclusions and discussions in Section 6.

2. Parameter mapping

For 2D problems, the boundary Γ of the domain Ω is represented by curves in parametric form exactly as the B-rep data structure in most CAD software. In the DiBFM, both boundary integration and dual interpolation are performed in parametric space of each curve.

A curve is represented in parametric form as:

$$\begin{cases} x_1 = x_1(\eta) \\ x_2 = x_2(\eta) \end{cases}, \qquad \eta \in [0,1], \tag{1}$$

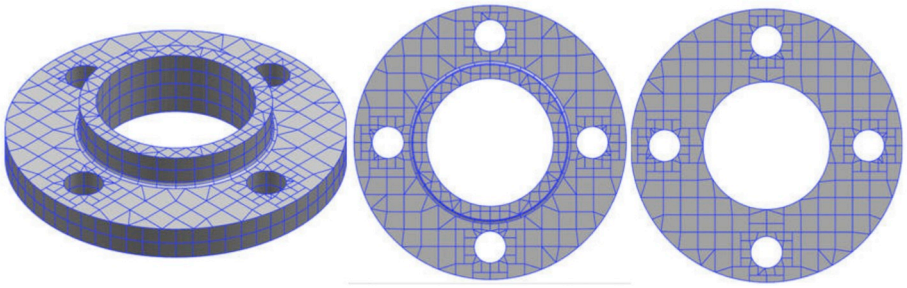

Fig. 2. Discontinuous surface girds of the flange plate.

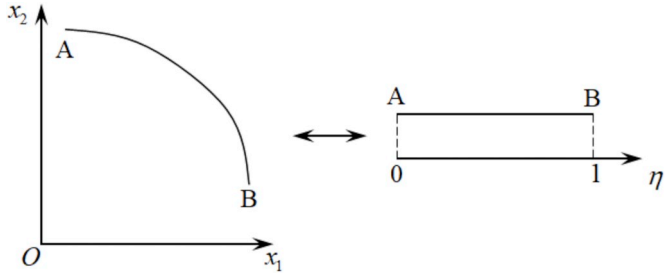

Fig. 3. Mapping between the Euclidean space and the parametric space.

where η is the parametric coordinate of curve (see Fig. 3). In this paper, a geometric map F: $\mathbb{R} \to \mathbb{R}^2$ is created by Eq. (1). The parametric coordinate η is obtained by the following linear transformation:

$$\eta = 0.5(\eta_b + \eta_a) + 0.5(\eta_b - \eta_a)\xi, \qquad \xi \in [-1,1], \tag{2}$$

where ξ is the intrinsic coordinate defined on the curve element, η_a and η_b are parametric coordinates of vertices of the curve element (see Fig. 4). If we obtain the parametric coordinate η in parametric space $\mathbb{R}$ located at the curve element, the coordinates (x_1, x_2) in Euclidean space $\mathbb{R}^2$ can be accurately calculated by Eq. (1). This means that the calculated point is located on the initial curve so that no geometric errors are introduced.

3. Dual interpolation method for elasticity problem

3.1. Dual interpolation element

As shown in Fig. 5, the nodes of a dual interpolation element are classified into two groups: source and virtual nodes. Taking into account both virtual and source nodes, it is equivalent to a standard conforming element. Ignoring virtual nodes, however, it becomes a conventional nonconforming element. Thus, the dual interpolation element is able to unify the conforming and nonconforming elements. Shape functions of the elements (a), (b) and (c) are:

$$N_1^s(\xi) = (1-\xi)(1-\xi) \text{ and } \begin{cases} N_1^v(\xi) = 0.5\xi(\xi-1) \\ N_2^v(\xi) = 0.5\xi(\xi+1) \end{cases}, \tag{3}$$

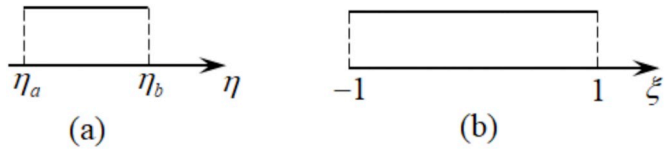

Fig. 4. Curve element: (a) in parametric space and (b) in space of intrinsic coordinates.

$$\begin{cases} N_1^s(\xi) = \frac{[\xi-(1-d)](\xi+1)(\xi-1)}{2d(1-d)(2-d)} \\ N_2^s(\xi) = -\frac{[\xi+(1-d)](\xi+1)(\xi-1)}{2d(1-d)(2-d)} \end{cases} \text{and} \begin{cases} N_1^v(\xi) = -\frac{[\xi+(1-d)][\xi-(1-d)](\xi-1)}{2d(2-d)} \\ N_2^v(\xi) = \frac{[\xi+(1-d)][\xi-(1-d)](\xi+1)}{2d(2-d)} \end{cases}, \tag{4}$$

$$\begin{cases} N_1^s(\xi) = -\frac{[\xi-(1-d)](\xi+1)(\xi-1)\xi}{2d(2-d)(1-d)^2} \\ N_2^s(\xi) = \frac{[\xi+(1-d)][\xi-(1-d)](\xi+1)(\xi-1)}{(1-d)^2} \\ N_3^s(\xi) = -\frac{[\xi+(1-d)](\xi+1)(\xi-1)\xi}{2d(2-d)(1-d)^2} \end{cases} \text{and} \begin{cases} N_1^v(\xi) = \frac{[\xi+(1-d)][\xi-(1-d)](\xi-1)\xi}{2d(2-d)} \\ N_2^v(\xi) = \frac{[\xi+(1-d)][\xi-(1-d)](\xi+1)\xi}{2d(2-d)} \end{cases}, \tag{5}$$

where d is the offset of source nodes, which is constrained to the interval (0, 1). In this paper, the value of d is taken to be 0.25.

3.2. First-layer interpolation

For 2D elasticity problems, the independent physical variables on the boundary are displacements u_i and tractions t_i (i = 1, 2). These variables in this study are approximated by dual interpolation elements (first-layer interpolation), which are performed in parametric space:

$$u_i(x_1, x_2) = u_i(\eta) = u_i(\xi) = \sum_{\alpha=1}^{n\alpha} N_\alpha^s(\xi) u_i(Q_\alpha^s) + \sum_{\beta=1}^{n\beta} N_\beta^v(\xi) u_i(Q_\beta^v), \tag{6}$$

$$t_i(x_1, x_2) = t_i(\eta) = t_i(\xi) = \sum_{\alpha=1}^{n\alpha} N_\alpha^s(\xi) t_i(Q_\alpha^s) + \sum_{\beta=1}^{n\beta} N_\beta^v(\xi) t_i(Q_\beta^v), \tag{7}$$

where $n\alpha$ and $n\beta$ are the total number of source and virtual nodes of dual interpolation element, respectively. $N_\alpha^s(\xi)$, $u_i(Q_\alpha^s)$ and $t_i(Q_\alpha^s)$ are the shape function, displacement and traction of the α^{th} source node in dual interpolation element, respectively. $N_\beta^v(\xi)$, $u_i(Q_\beta^v)$ and $t_i(Q_\beta^v)$ are the shape function, displacement and traction of the β^{th} virtual node on dual interpolation element, respectively. In this study, we will use the second-layer interpolation to calculate $u_i(Q_\beta^v)$ and $t_i(Q_\beta^v)$, because these nodal values are not independent variables.

3.3. Second-layer interpolation

The MLS approximation is adopted for the second-layer interpolation. In the proposed method, it is just used to construct the relationships between source and virtual nodes. Due to the fact that our method has the topological relationships between the nodes and elements, the source nodes covered in the influence domain of a virtual node can be obtained by directly searching the neighboring three layer elements (see Figs. 6–8).

As shown in Fig. 1(d), one virtual node is placed at a point where two adjacent elements are smoothly connected, letting the two elements share a same virtual node. However, two virtual nodes are placed at geometric corner or point which boundary condition is

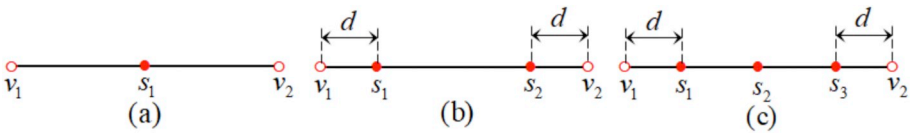

Fig. 5. Dual interpolation elements for 2D problems: (a) constant, (b) linear, and (c) quadratic.

discontinuous, one for each element. Unlike the multiple-node method (Mitra and Ingber, 1993), the BIE is not collocated at virtual nodes in the DiBFM. Obviously, the two virtual nodes cannot lead to a pair of linearly dependent equations no matter what boundary conditions are imposed on two adjacent edges.

For virtual node Q_β^v at smooth boundaries (see Fig. 6), the second-layer interpolation for $u_i(Q_\beta^v)$ and $t_i(Q_\beta^v)$ are defined as:

$$u_i(Q_\beta^v) = \sum_{m=1}^{M} \phi_m^{vs}\left(\eta_\beta^v\right) u_i(Q_m^s), \tag{8}$$

$$t_i(Q_\beta^v) = \sum_{m=1}^{M} \phi_m^{vs}\left(\eta_\beta^v\right) t_i(Q_m^s), \tag{9}$$

where η_β^v is the parametric coordinate of virtual node Q_β^v, M is the total number of source nodes Q_m^s covered in the influence domain of Q_β^v, $u_i(Q_m^s)$ and $t_i(Q_m^s)$ are displacement and traction of source node Q_m^s, respectively. $\phi_m^{vs}\left(\eta_\beta^v\right)$ is the shape function of second-layer interpolation corresponding to source node Q_m^s:

$$\phi_m^{vs}\left(\eta_\beta^v\right) = \sum_{n=1}^{M} \psi_n^{vs}\left(\eta_\beta^v\right)\left[(\mathbf{\Psi}^{ss})^{-1}\right]_{nm}, \tag{10}$$

in which

$$\mathbf{\Psi}^{ss} = [\psi_n^{ss}(\eta_m^s)],$$

where η_m^s is the parametric coordinate of source node Q_m^s, $\psi_n^{vs}\left(\eta_\beta^v\right)$ and $\psi_n^{ss}(\eta_m^s)$ are the shape functions of MLS approximation corresponding to source node Q_m^s. The details of the MLS approximation are available in Ref. (Lancaster and Salkauskas, 1981).

For virtual node Q_β^v at geometric corner or point which boundary condition is discontinuous (see Figs. 7 and 8), $t_i(Q_\beta^v)$ is also calculated by Eq. (9). $u_i(Q_\beta^v)$ is calculated by:

$$u_i(Q_\beta^v) = u_i(\bar{Q}_\beta^v) = \sum_{m=1}^{M} \omega(Q_\beta^v)\phi_m^{vs}\left(\eta_\beta^v\right) u_i(Q_m^s) + \sum_{m=1}^{\bar{M}} \omega(\bar{Q}_\beta^v)\phi_m^{vs}\left(\bar{\eta}_\beta^v\right) u_i(\bar{Q}_m^s), \tag{11}$$

in which

$$\omega(Q_\beta^v) = \frac{L(\bar{Q}_\beta^v)}{L(Q_\beta^v) + L(\bar{Q}_\beta^v)} \quad \text{and} \quad \omega(\bar{Q}_\beta^v) = \frac{L(Q_\beta^v)}{L(Q_\beta^v) + L(\bar{Q}_\beta^v)},$$

$$L(Q_\beta^v) = \min_{1\le m\le M}\{\|Q_\beta^v - Q_m^s\|\} \quad \text{and} \quad L(\bar{Q}_\beta^v) = \min_{1\le m\le \bar{M}}\{\|\bar{Q}_\beta^v - \bar{Q}_m^s\|\},$$

where $\bar{Q}_\beta^v$ is a virtual node which is at the same geometric location for virtual node Q_β^v (see Fig. 7), and $\|\cdot\|$ denotes the arc length in $\mathbb{R}^2$.

From Eqs. (8), (9) and (11), the displacements and tractions can be naturally and accurately approximated by manipulating the influence domains of some specific virtual nodes in the second-layer interpolation (see Figs. 6–8). Fig. 9 shows the algorithm of dual interpolation method.

As pointed out in Ref. (Belytschko et al., 1994), the Gaussian-type weight functions yield excellent results. In this study, we use the following Gaussian weight function:

$$w_n(\bar{\eta}) = \begin{cases} \dfrac{e^{-(d_n/c_n)^2} - e^{-(\hat{d}_n/c_n)^2}}{1 - e^{-(\hat{d}_n/c_n)^2}}, & 0 \le d_n \le \hat{d}_n \\ 0, & d_n \ge \hat{d}_n \end{cases}, \tag{12}$$

in which

$$d_n = |\eta_n^s - \bar{\eta}|,$$

where $\bar{\eta}$ can either be the parametric coordinate of virtual node Q_β^v or the parametric coordinate of source node Q_m^s, c_n is a constant controlling the shape of the weight function, is the size of the support for the weight function $w_n(\bar{\eta})$. In this paper, is defined as:

$$\hat{d}_n = scale \times l_{\max}, \tag{13}$$

in which

$$sacle = \begin{cases} 1, & \text{when only one layer souce nodes are adjacent to virtual node } Q_\beta^v \\ 2, & \text{when only two layer souce nodes are adjacent to virtual node } Q_\beta^v \\ 3, & \text{when at least three layer souce nodes are adjacent to virtual node } Q_\beta^v \end{cases},$$

where $l_{\max}$ is the maximum length of the cells connected to virtual node Q_β^v, in parametric space $\mathbb{R}$ (see Fig. 6).

Because the stability of the MLS approximation deteriorates severely as the nodal spacing decreases, the following quadratic basis is used (Li and Li, 2016):

$$\mathbf{p}^{\mathrm{T}}(\eta, \bar{\eta}) = \left[1, \frac{\eta_n^s - \bar{\eta}}{h}, \left(\frac{\eta_n^s - \bar{\eta}}{h}\right)^2\right], \tag{14}$$

in which

$$h = \max_{1\le m\le M} \min_{1\le n\le M, m\ne n} |\eta_n^s - \eta_m^s|.$$

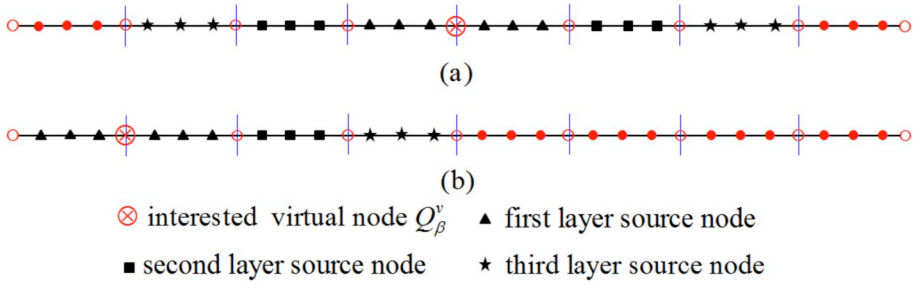

Fig. 6. Influence domain of an interested virtual node Q_β^v, for Q_β^v located at smooth boundaries.

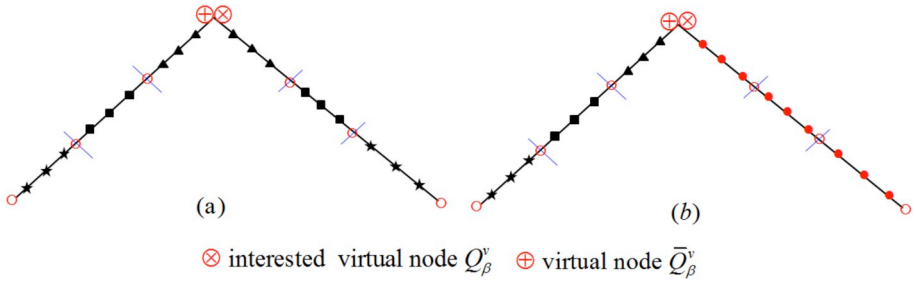

Fig. 7. Influence domain of an interested virtual node Q_β^v at geometric corner: (a) for approximating displacements and (b) for approximating tractions.

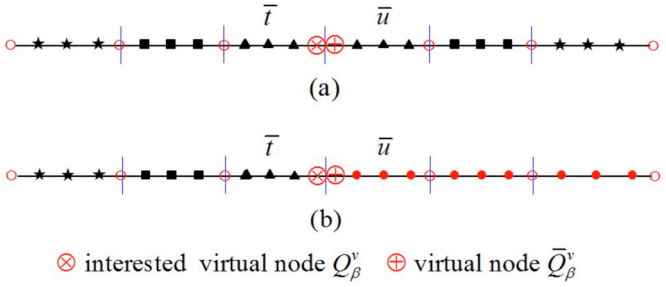

Fig. 8. Influence domain of an interested virtual node Q_β^v at point which boundary condition is discontinuous: (a) for approximating displacements and (b) for approximating tractions.

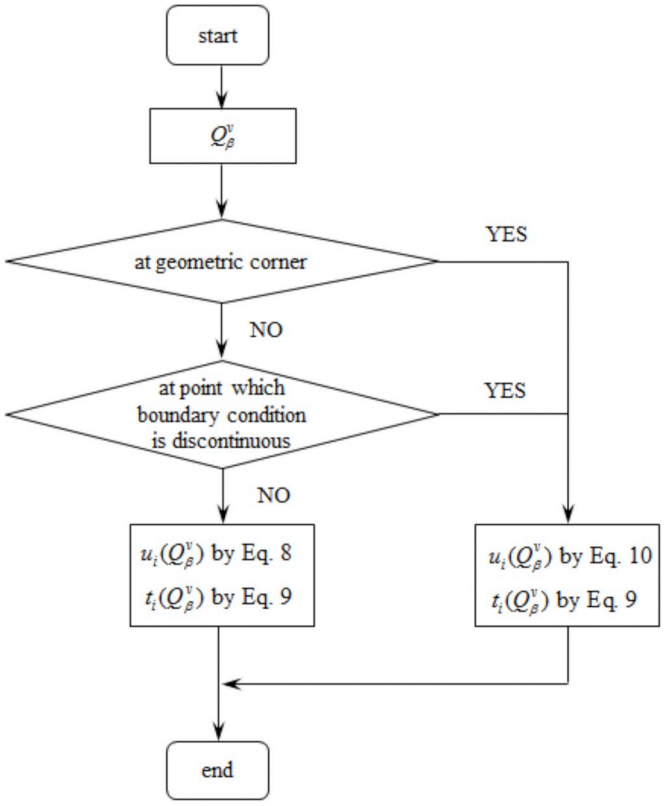

Fig. 9. Flow chart of dual interpolation method.

4. DiBFM for elasticity problem

4.1. Boundary integral equation

Consider the elasticity problem in a 2D finite domain Ω with the boundary Γ. The boundary integral equation (BIE) for the elasticity problem is:

$$c_{ij}(P)u_j(P) = \int_\Gamma U_{ij}(P, Q)t_j(Q)d\Gamma(Q) - \int_\Gamma T_{ij}(P, Q)u_j(Q)d\Gamma(Q), \quad P, Q \in \Gamma, \tag{15}$$

where u_j and t_j ($j = 1, 2$) are the displacement and traction components, respectively. The coefficient $c_{ij}(P) = 1/2\delta_{ij}$ if Γ is smooth at source node P. For plane-strain problems, $U_{ij}(P, Q)$ and $T_{ij}(P, Q)$ are:

$$U_{ij}(P, Q) = \frac{1}{8\pi\mu(1-\nu)}\left[(3-4\nu)\delta_{ij}\ln\frac{1}{r} + r_{,i}r_{,j}\right], \tag{16}$$

$$T_{ij}(P, Q) = -\frac{1}{4\pi(1-\nu)r}\left\{\frac{\partial r}{\partial n}[(1-2\nu)\delta_{ij} + 2r_{,i}r_{,j}] - (1-2\nu)(r_{,i}n_j - r_{,j}n_i)\right\}, \tag{17}$$

where r is the distance between the source node P and field point Q, n is the outward normal at the field point Q, n_i and n_j are the components of n, μ and ν are the shear modulus and the Poisson's ratio, respectively.

4.2. Discretization of the BIE for elasticity problems

In the DiBFM, the BIE is discretized by dual interpolation elements, but we collocate the BIE only at source nodes P_k (k = 1,2, …, NS). The discretization form of the BIE for elasticity problems is:

$$\sum_{e=1}^{ne}\left[\sum_{\alpha=1}^{n\alpha} h_{ij}^{ss}(P_k)u_j(Q_{e(\alpha)}^s) + \sum_{\beta=1}^{n\beta} h_{ij}^{sv}(P_k)u_j(Q_{e(\beta)}^v)\right] = \sum_{e=1}^{ne}\left[\sum_{\alpha=1}^{n\alpha} g_{ij}^{ss}(P_k)t_j(Q_{e(\alpha)}^s) + \sum_{\beta=1}^{n\beta} g_{ij}^{sv}(P_k)t_j(Q_{e(\beta)}^v)\right], \tag{18}$$

in which

$$h_{ij}^{ss}(P_k) = \int_{\Gamma_e} T_{ij}(P_k, Q)N_{e(\alpha)}^s(Q)d\Gamma(Q) + \frac{1}{2}\delta_{ij}\delta_{e(\alpha)}^k,$$

$$h_{ij}^{sv}(P_k) = \int_{\Gamma_e} T_{ij}(P_k, Q)N_{e(\beta)}^v(Q)d\Gamma(Q),$$

$$g_{ij}^{ss}(P_k) = \int_{\Gamma_e} U_{ij}(P_k, Q)N_{e(\alpha)}^s(Q)d\Gamma(Q),$$

$$g_{ij}^{sv}(P_k) = \int_{\Gamma_e} U_{ij}(P_k, Q)N_{e(\beta)}^v(Q)d\Gamma(Q),$$

and

$$\delta_{e(\alpha)}^k = \begin{cases} 1, & \text{if source node } P_k \text{ is the } \alpha^{\text{th}} \text{ source node in the } e^{\text{th}} \text{ element} \\ 0 \end{cases},$$

where Γ_e denotes the boundary of domain corresponding to eth element, $N_{e(\alpha)}^s$, $u_j(Q_{e(\alpha)}^s)$ and $t_j(Q_{e(\alpha)}^s)$ are the shape function, displacement and traction of α^{th} source node in eth element, respectively. $N_{e(\beta)}^v$, $u_j(Q_{e(\beta)}^v)$ and $t_j(Q_{e(\beta)}^v)$ are the shape function, displacement and traction of β^{th} virtual node on eth element, respectively.

The matrix form of Eq. (18) is:

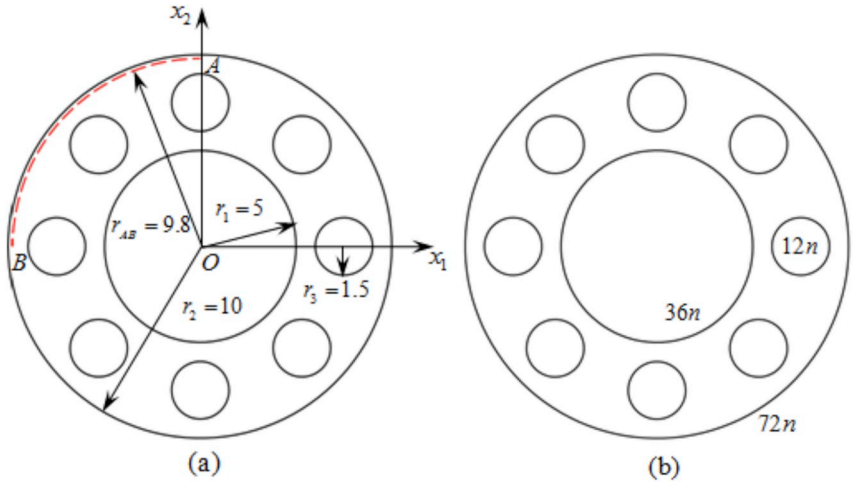

Fig. 10. Displacement field problem: (a) geometric model and (b) the number of source nodes on each edge (n = 1, 3, 6, 9, 12).

Table 1
Numerical results for displacement field problem.

DiBFM					BEM				
NE	*NS*	*Err_t*$_1$	*Err_t*$_2$	*Time* (s)	*NE*	*NS*	*Err_t*$_1$	*Err_t*$_2$	*Time* (s)
102	204	5.05e-03	4.47e-03	38.47	204	204	2.33e-02	2.33e-02	29.86
306	612	1.07e-04	1.12e-04	121.98	612	612	1.92e-03	1.92e-03	101.87
612	1224	1.14e-05	1.11e-05	275.71	1224	1224	4.38e-04	4.38e-04	235.26
918	1836	3.05e-06	2.91e-06	457.37	1836	1836	1.89e-04	1.89e-04	385.73
1224	2448	1.21e-06	1.15e-06	676.28	2448	2448	1.05e-04	1.05e-04	572.94

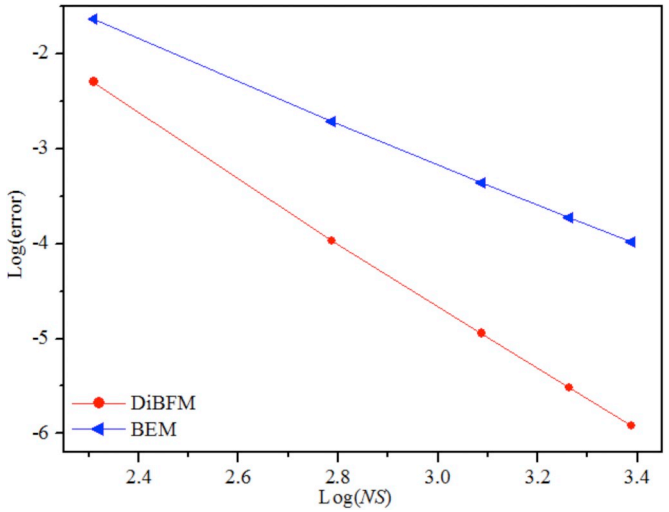

Fig. 11. Relative errors of traction t_1.

$$\begin{bmatrix}\mathbf{H}_{11}^{ss} & \mathbf{H}_{12}^{ss}\\ \mathbf{H}_{21}^{ss} & \mathbf{H}_{22}^{ss}\end{bmatrix}\begin{Bmatrix}\mathbf{u}_1^s\\ \mathbf{u}_2^s\end{Bmatrix}+\begin{bmatrix}\mathbf{H}_{11}^{sv} & \mathbf{H}_{12}^{sv}\\ \mathbf{H}_{21}^{sv} & \mathbf{H}_{22}^{sv}\end{bmatrix}\begin{Bmatrix}\mathbf{u}_1^v\\ \mathbf{u}_2^v\end{Bmatrix}=\begin{bmatrix}\mathbf{G}_{11}^{ss} & \mathbf{G}_{12}^{ss}\\ \mathbf{G}_{21}^{ss} & \mathbf{G}_{22}^{ss}\end{bmatrix}\begin{Bmatrix}\mathbf{t}_1^s\\ \mathbf{t}_2^s\end{Bmatrix}+\begin{bmatrix}\mathbf{G}_{11}^{sv} & \mathbf{G}_{12}^{sv}\\ \mathbf{G}_{21}^{sv} & \mathbf{G}_{22}^{sv}\end{bmatrix}\begin{Bmatrix}\mathbf{t}_1^v\\ \mathbf{t}_2^v\end{Bmatrix}, \tag{19}$$

where $\mathbf{u}_j^s$ and $\mathbf{t}_j^s$ are displacement and traction vectors containing all source nodes, respectively. $\mathbf{u}_j^v$ and $\mathbf{t}_j^v$ are displacement and traction vectors containing all virtual nodes, respectively. $\mathbf{H}_{ij}^{ss}$, $\mathbf{G}_{ij}^{ss}$, $\mathbf{H}_{ij}^{sv}$ and $\mathbf{G}_{ij}^{sv}$ are the coefficient matrices corresponding to vectors $\mathbf{u}_j^s$, $\mathbf{t}_j^s$, $\mathbf{u}_j^v$ and $\mathbf{t}_j^v$, respectively. Because these vectors contain known and unknown variables, Eq. (19) can be rewritten as:

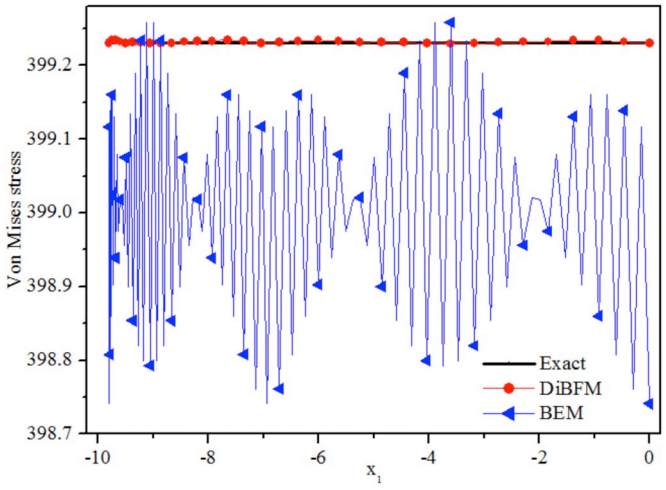

Fig. 12. Von Mises stress along the curve *AB*.

$$\begin{bmatrix}\mathbf{H}_{1d_1}^{ss} & \mathbf{H}_{1n_1}^{ss} & \mathbf{H}_{1d_2}^{ss} & \mathbf{H}_{1n_2}^{ss}\\ \mathbf{H}_{2d_1}^{ss} & \mathbf{H}_{2n_1}^{ss} & \mathbf{H}_{2d_2}^{ss} & \mathbf{H}_{2n_2}^{ss}\end{bmatrix}\begin{Bmatrix}\bar{\mathbf{u}}_{d_1}^s\\ \mathbf{u}_{n_1}^s\\ \bar{\mathbf{u}}_{d_2}^s\\ \mathbf{u}_{n_2}^s\end{Bmatrix}+\begin{bmatrix}\mathbf{H}_{1d_1}^{sv} & \mathbf{H}_{1n_1}^{sv} & \mathbf{H}_{1d_2}^{sv} & \mathbf{H}_{1n_2}^{sv}\\ \mathbf{H}_{2d_1}^{sv} & \mathbf{H}_{2n_1}^{sv} & \mathbf{H}_{2d_2}^{sv} & \mathbf{H}_{2n_2}^{sv}\end{bmatrix}\begin{Bmatrix}\bar{\mathbf{u}}_{d_1}^v\\ \mathbf{u}_{n_1}^v\\ \bar{\mathbf{u}}_{d_2}^v\\ \mathbf{u}_{n_2}^v\end{Bmatrix}$$
$$=\begin{bmatrix}\mathbf{G}_{1d_1}^{ss} & \mathbf{G}_{1n_1}^{ss} & \mathbf{G}_{1d_2}^{ss} & \mathbf{G}_{1n_2}^{ss}\\ \mathbf{G}_{2d_1}^{ss} & \mathbf{G}_{2n_1}^{ss} & \mathbf{G}_{2d_2}^{ss} & \mathbf{G}_{2n_2}^{ss}\end{bmatrix}\begin{Bmatrix}\mathbf{t}_{d_1}^s\\ \bar{\mathbf{t}}_{n_1}^s\\ \mathbf{t}_{d_2}^s\\ \bar{\mathbf{t}}_{n_2}^s\end{Bmatrix}+\begin{bmatrix}\mathbf{G}_{1d_1}^{sv} & \mathbf{G}_{1n_1}^{sv} & \mathbf{G}_{1d_2}^{sv} & \mathbf{G}_{1n_2}^{sv}\\ \mathbf{G}_{2d_1}^{sv} & \mathbf{G}_{2n_1}^{sv} & \mathbf{G}_{2d_2}^{sv} & \mathbf{G}_{2n_2}^{sv}\end{bmatrix}\begin{Bmatrix}\mathbf{t}_{d_1}^v\\ \bar{\mathbf{t}}_{n_1}^v\\ \mathbf{t}_{d_2}^v\\ \bar{\mathbf{t}}_{n_2}^v\end{Bmatrix} \tag{20}$$

where the subscripts d_j and n_j stand for the boundary conditions of Dirichlet and Neumann type, respectively. $\bar{\mathbf{u}}_{d_j}^s$ and $\bar{\mathbf{u}}_{d_j}^v$ are the known

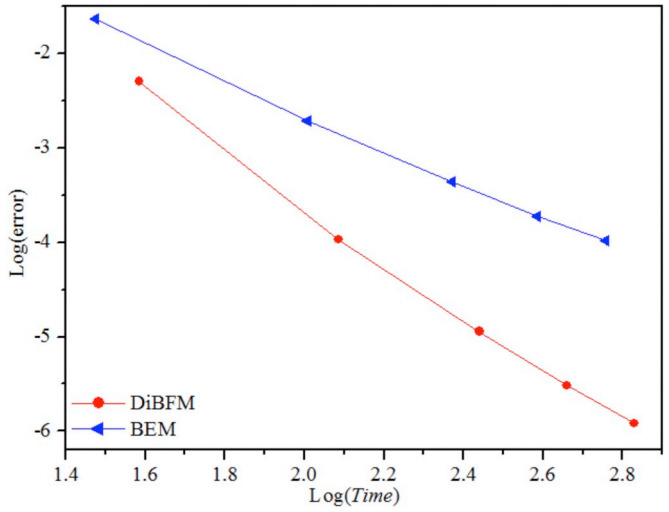

Fig. 13. Comparison of computational efficiency for traction t_1.

displacement vectors containing source and virtual nodes of Dirichlet boundary conditions, respectively. $\bar{\mathbf{t}}^s_{nj}$ and $\bar{\mathbf{t}}^v_{nj}$ are the known traction vectors containing source and virtual nodes of Neumann boundary conditions, respectively.

4.3. Condensation of degrees of freedom for virtual nodes

Since the BIEs are collocated at source nodes only, the number of linear algebraic equations is less than the number of unknown nodal values (see Eq. (20)). To make the final system of linear equations solvable, additional constraint equations are required to condense the degrees of freedom for virtual nodes. The matrix forms of these equations are:

$$\begin{Bmatrix} \mathbf{u}^v_{n_1} \\ \mathbf{u}^v_{n_2} \end{Bmatrix} = \begin{bmatrix} \boldsymbol{\Psi}^{vs}_{n_1 d_1} & \boldsymbol{\Psi}^{vs}_{n_1 n_1} & & \\ & & \boldsymbol{\Psi}^{vs}_{n_2 d_2} & \boldsymbol{\Psi}^{vs}_{n_2 n_2} \end{bmatrix} \begin{Bmatrix} \bar{\mathbf{u}}^s_{d_1} \\ \mathbf{u}^s_{n_1} \\ \bar{\mathbf{u}}^s_{d_2} \\ \mathbf{u}^s_{n_2} \end{Bmatrix}, \tag{21}$$

$$\begin{Bmatrix} \mathbf{t}^v_{d_1} \\ \mathbf{t}^v_{d_2} \end{Bmatrix} = \begin{bmatrix} \boldsymbol{\Theta}^{vs}_{d_1 d_1} & \\ & \boldsymbol{\Theta}^{vs}_{d_2 d_2} \end{bmatrix} \begin{Bmatrix} \mathbf{t}^s_{d_1} \\ \mathbf{t}^s_{d_2} \end{Bmatrix}, \tag{22}$$

where $\boldsymbol{\Psi}^{vs}_{njdj}$, $\boldsymbol{\Psi}^{vs}_{njnj}$ and $\boldsymbol{\Theta}^{vs}_{djdj}$ are shape function matrices of the second-layer interpolation, which are constructed by the MLS approximation descript in Section 3.3.

Substituting Eqs. (21) and (22) into Eq. (20) yields:

$$\begin{bmatrix} \bar{\mathbf{H}}^{ss}_{1d_1} & \bar{\mathbf{H}}^{ss}_{1n_1} & \bar{\mathbf{H}}^{ss}_{1d_2} & \bar{\mathbf{H}}^{ss}_{1n_2} \\ \bar{\mathbf{H}}^{ss}_{2d_1} & \bar{\mathbf{H}}^{ss}_{2n_1} & \bar{\mathbf{H}}^{ss}_{2d_2} & \bar{\mathbf{H}}^{ss}_{2n_2} \end{bmatrix} \begin{Bmatrix} \bar{\mathbf{u}}^s_{d_1} \\ \mathbf{u}^s_{n_1} \\ \bar{\mathbf{u}}^s_{d_2} \\ \mathbf{u}^s_{n_2} \end{Bmatrix} + \begin{bmatrix} \mathbf{H}^{sv}_{1d_1} & \mathbf{H}^{sv}_{1d_2} \\ \mathbf{H}^{sv}_{2d_1} & \mathbf{H}^{sv}_{2d_2} \end{bmatrix} \begin{Bmatrix} \bar{\mathbf{u}}^v_{d_1} \\ \bar{\mathbf{u}}^v_{d_2} \end{Bmatrix}$$
$$= \begin{bmatrix} \bar{\mathbf{G}}^{ss}_{1d_1} & \mathbf{G}^{ss}_{1n_1} & \bar{\mathbf{G}}^{ss}_{1d_2} & \mathbf{G}^{ss}_{1n_2} \\ \bar{\mathbf{G}}^{ss}_{2d_1} & \mathbf{G}^{ss}_{2n_1} & \bar{\mathbf{G}}^{ss}_{2d_2} & \mathbf{G}^{ss}_{2n_2} \end{bmatrix} \begin{Bmatrix} \mathbf{t}^s_{d_1} \\ \bar{\mathbf{t}}^s_{n_1} \\ \mathbf{t}^s_{d_2} \\ \bar{\mathbf{t}}^s_{n_2} \end{Bmatrix} + \begin{bmatrix} \mathbf{G}^{sv}_{1n_1} & \mathbf{G}^{sv}_{1n_2} \\ \mathbf{G}^{sv}_{2n_1} & \mathbf{G}^{sv}_{2n_2} \end{bmatrix} \begin{Bmatrix} \bar{\mathbf{t}}^v_{n_1} \\ \bar{\mathbf{t}}^v_{n_2} \end{Bmatrix} \tag{23}$$

in which

$$\begin{bmatrix} \bar{\mathbf{H}}^{ss}_{1d_1} & \bar{\mathbf{H}}^{ss}_{1n_1} \\ \bar{\mathbf{H}}^{ss}_{2d_1} & \bar{\mathbf{H}}^{ss}_{2n_1} \end{bmatrix} = \begin{bmatrix} \mathbf{H}^{ss}_{1d_1} & \mathbf{H}^{ss}_{1n_1} \\ \mathbf{H}^{ss}_{2d_1} & \mathbf{H}^{ss}_{2n_1} \end{bmatrix} + \begin{bmatrix} \mathbf{H}^{sv}_{1n_1} \\ \mathbf{H}^{sv}_{2n_1} \end{bmatrix} \begin{bmatrix} \boldsymbol{\Psi}^{vs}_{n_1 d_1} & \boldsymbol{\Psi}^{vs}_{n_1 n_1} \end{bmatrix},$$

$$\begin{bmatrix} \bar{\mathbf{H}}^{ss}_{1d_2} & \bar{\mathbf{H}}^{ss}_{1n_2} \\ \bar{\mathbf{H}}^{ss}_{2d_2} & \bar{\mathbf{H}}^{ss}_{2n_2} \end{bmatrix} = \begin{bmatrix} \mathbf{H}^{ss}_{1d_2} & \mathbf{H}^{ss}_{1n_2} \\ \mathbf{H}^{ss}_{2d_2} & \mathbf{H}^{ss}_{2n_2} \end{bmatrix} + \begin{bmatrix} \mathbf{H}^{sv}_{1n_2} \\ \mathbf{H}^{sv}_{2n_2} \end{bmatrix} \begin{bmatrix} \boldsymbol{\Psi}^{vs}_{n_2 d_2} & \boldsymbol{\Psi}^{vs}_{n_2 n_2} \end{bmatrix},$$

$$\begin{bmatrix} \bar{\mathbf{G}}^{ss}_{1d_1} \\ \bar{\mathbf{G}}^{ss}_{2d_1} \end{bmatrix} = \begin{bmatrix} \mathbf{G}^{ss}_{1d_1} \\ \mathbf{G}^{ss}_{2d_1} \end{bmatrix} + \begin{bmatrix} \mathbf{G}^{sv}_{1d_1} \\ \mathbf{G}^{sv}_{2d_1} \end{bmatrix} \boldsymbol{\Theta}^{vs}_{d_1 d_1},$$

$$\begin{bmatrix} \bar{\mathbf{G}}^{ss}_{1d_2} \\ \bar{\mathbf{G}}^{ss}_{2d_2} \end{bmatrix} = \begin{bmatrix} \mathbf{G}^{ss}_{1d_2} \\ \mathbf{G}^{ss}_{2d_2} \end{bmatrix} + \begin{bmatrix} \mathbf{G}^{sv}_{1d_2} \\ \mathbf{G}^{sv}_{2d_2} \end{bmatrix} \boldsymbol{\Theta}^{vs}_{d_2 d_2}.$$

4.4. Solution for elasticity problems

Applying the boundary conditions at each source and virtual nodes and switching the columns of matrices in Eq. (23), a standard system of linear equations as follows is formed:

$$\mathbf{A}\mathbf{x} = \mathbf{b}, \tag{24}$$

in which

$$\mathbf{A} = \begin{bmatrix} -\bar{\mathbf{G}}^{ss}_{1d_1} & \bar{\mathbf{H}}^{ss}_{1n_1} & -\bar{\mathbf{G}}^{ss}_{1d_2} & \bar{\mathbf{H}}^{ss}_{1n_2} \\ -\bar{\mathbf{G}}^{ss}_{2d_1} & \bar{\mathbf{H}}^{ss}_{2n_1} & -\bar{\mathbf{G}}^{ss}_{2d_2} & \bar{\mathbf{H}}^{ss}_{2n_2} \end{bmatrix},$$

$$\mathbf{x} = \left\{ \mathbf{t}^s_{d_1} \quad \mathbf{u}^s_{n_1} \quad \mathbf{t}^s_{d_2} \quad \mathbf{u}^s_{n_2} \right\}^{\mathrm{T}},$$

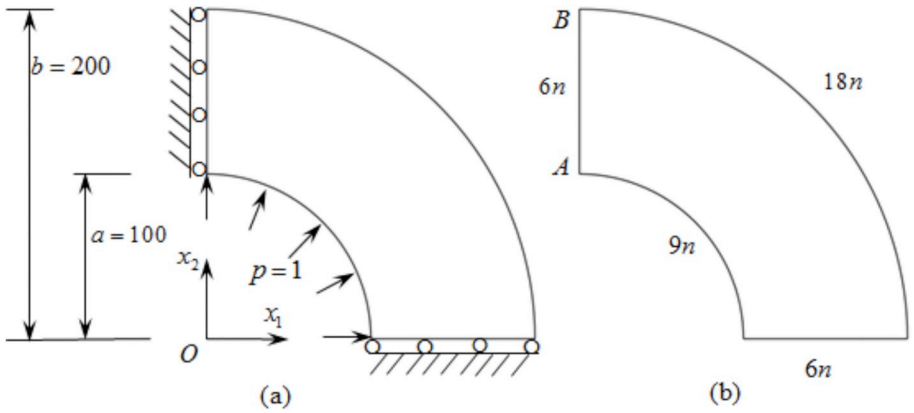

Fig. 14. Thick-wall cylinder under internal pressure: (a) geometric model and boundary conditions; and (b) the number of source nodes on each edge (n = 1, 2, 4, 8, 16).

Table 2
Numerical results for thick-wall cylinder under internal pressure.

DiBFM						BEM					
NE	*NS*	*Err_u_r*	*Err_σ_r*	*Err_σ_θ*	*Time* (s)	*NE*	*NS*	*Err_u_r*	*Err_σ_r*	*Err_σ_θ*	*Time* (s)
13	39	3.67e-05	1.12e-03	9.68e-04	3.58	19	42	1.33e-03	1.16e-02	4.23e-03	3.29
26	78	7.51e-06	4.52e-04	1.03e-04	7.53	39	82	1.22e-04	3.17e-03	8.02e-04	6.60
52	156	9.98e-07	1.17e-04	1.45e-05	16.23	78	160	1.56e-05	7.94e-04	1.97e-04	13.99
104	312	1.22e-07	2.71e-05	2.68e-06	35.49	156	316	1.98e-06	1.96e-04	4.90e-05	30.81
208	624	1.44e-08	5.89e-06	5.36e-07	80.27	312	628	2.49e-07	4.86e-05	1.22e-05	69.91

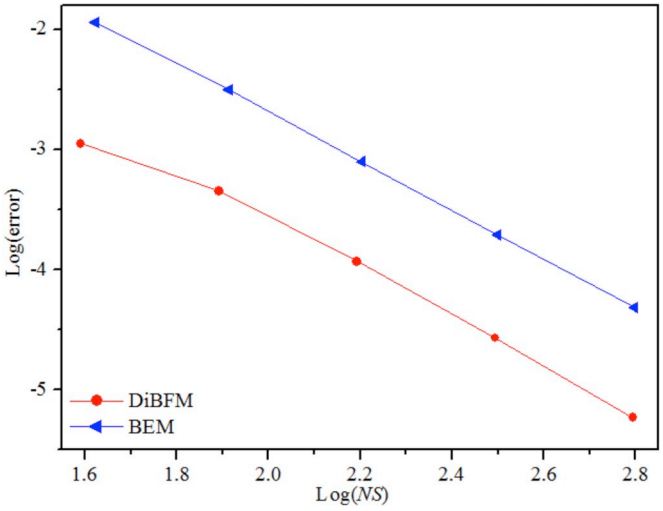

Fig. 15. Relative errors of radial stress σ_r.

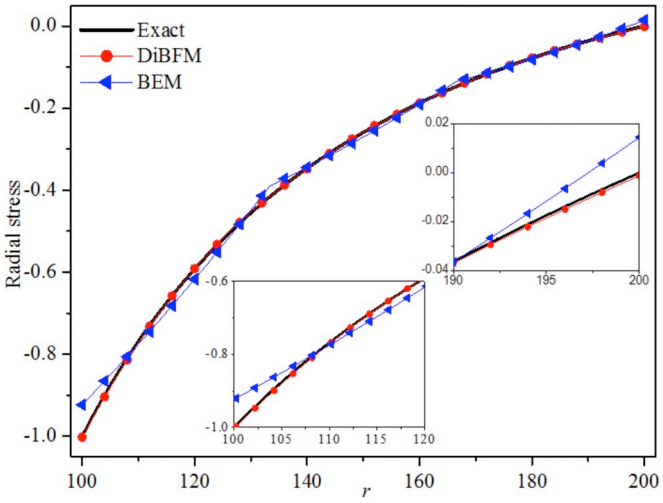

Fig. 16. Radial stress σ_r along the edge *AB*.

$$\mathbf{b} = \begin{bmatrix} -\bar{\mathbf{H}}^{ss}_{1d_1} & \mathbf{G}^{ss}_{1n_1} & -\bar{\mathbf{H}}^{ss}_{1d_2} & \mathbf{G}^{ss}_{1n_2} \\ -\bar{\mathbf{H}}^{ss}_{2d_1} & \mathbf{G}^{ss}_{2n_1} & -\bar{\mathbf{H}}^{ss}_{2d_2} & \mathbf{G}^{ss}_{2n_2} \end{bmatrix} \begin{Bmatrix} \bar{\mathbf{u}}^{s}_{d_1} \\ \bar{\mathbf{t}}^{s}_{n_1} \\ \bar{\mathbf{u}}^{s}_{d_2} \\ \bar{\mathbf{t}}^{s}_{n_2} \end{Bmatrix} + \begin{bmatrix} -\mathbf{H}^{sv}_{1d_1} & \mathbf{G}^{sv}_{1n_1} & -\mathbf{H}^{sv}_{1d_2} & \mathbf{G}^{sv}_{1n_2} \\ -\mathbf{H}^{sv}_{2d_1} & \mathbf{G}^{sv}_{2n_1} & -\mathbf{H}^{sv}_{2d_2} & \mathbf{G}^{sv}_{2n_2} \end{bmatrix} \begin{Bmatrix} \bar{\mathbf{u}}^{v}_{d_1} \\ \bar{\mathbf{t}}^{v}_{n_1} \\ \bar{\mathbf{u}}^{v}_{d_2} \\ \bar{\mathbf{t}}^{v}_{n_2} \end{Bmatrix},$$

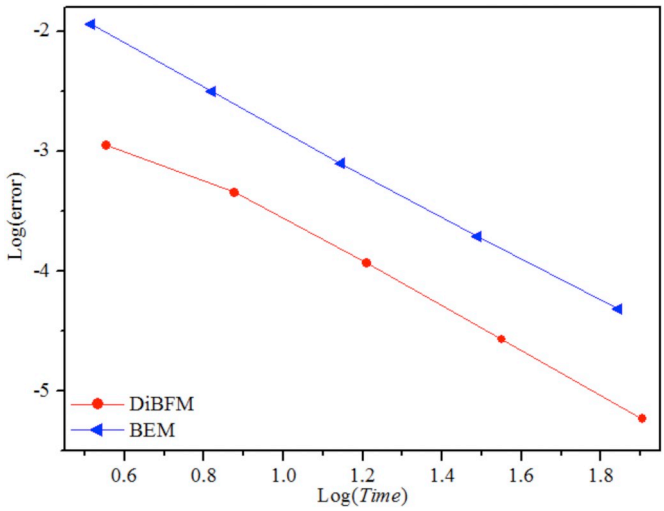

Fig. 17. Comparison of computational efficiency for radial stress σ_r.

where **A** is the coefficient matrix of dimensions $2NS \times 2NS$ for 2D elasticity problems, and **b** is the known right-hand-side vector. **x** is the unknown vector only containing source nodes.

Using the LU decomposition to solve Eq. (24), we can obtain all unknown values of source nodes in each dual interpolation element. Then, all unknown values of virtual nodes on each dual interpolation element are calculated by the second-layer interpolation, namely, Eqs. (21) and (22).

For the same number of source nodes, the size of the overall system of linear equations in the DiBFM is the same as that in the conventional BEM (see Eq. (24)), while the DiBFM is able to obtain higher computational accuracy. This is a major advantage of our method. The reasons for this are: (i) both displacements and tractions can be accurately approximated by dual interpolation method; (ii) the application of the boundary conditions in our method is more accurate than that in the conventional BEM; and (iii) the geometric data in the DiBFM are directly calculated from the curves to eliminate geometric errors (see Eq. (1)).

5. Numerical examples

In this section, four numerical examples are given to demonstrate the accuracy and efficiency of the DiBFM for solving 2D elasticity problems. All computations were done on a desktop computer with an Intel Core i7-4790 CPU (3.6-GHz) and 12 GB memory.

For the purpose of error estimation and convergence study, the relative error is defined as:

$$error = \frac{1}{|v|_{\max}} \sqrt{\frac{1}{M} \sum_{i=1}^{M} [v_i^{(e)} - v_i^{(n)}]^2}, \tag{25}$$

where $|v|_{\max}$ is the maximum value of displacement u_i or traction t_i over M sample points, and the superscripts (e) and (n) refer to the exact and

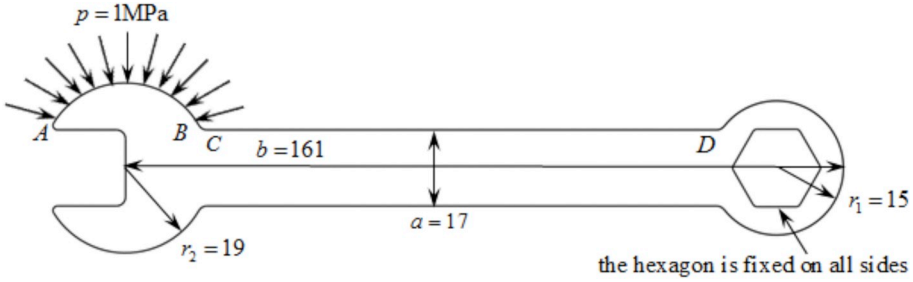

Fig. 18. Combination wrench: geometric model and boundary conditions.

Table 3
Numerical results for combination wrench.

DiBFM			FEM		
NE	*NS*	*Max_Mises* (MPa)	*NE*	*NS*	*Max_Mises* (MPa)
116	348	147.6142	1099	2409	139.6564
238	714	147.7179	6891	14,287	140.7536
476	1428	147.7289	2,6801	54,601	147.2225
714	2142	147.7317	106,769	215,531	148.6239
833	2499	147.7318	712,649	1,430,279	148.5471
952	2856	147.7317	1,936,667	3,881,639	148.4157

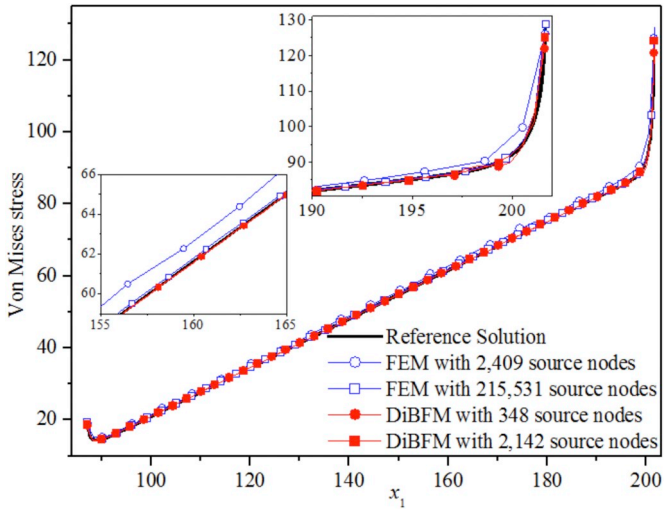

Fig. 19. Von Mises stress along the edge *CD*.

numerical solutions, respectively.

In all computations, unless indicated otherwise, the parameter d in Eqs. (4) and (5) is taken to be 0.25, the parameter $\hat{d}_n/c_n$ in Eq. (12) is a constant and equals to 2.0.

In the following figures and tables, symbols *NE* and *NS* are the total number of elements and source nodes, respectively. The CPU time spent in constructing and solving the system equations is denoted as *Time*. The maximum value of Von Mises stresses is denoted as *Max_Mises*.

5.1. Displacement field problem

The first example is a displacement field problem on a structure, which is constituted by a set of circles with different radius (see Fig. 10 (a)). Plane strain cases with Young's modulus $E = 1$ (in consistent units) and Poisson's ratio $\nu = 0.25$ are considered. The displacement fields imposed on all edges are:

$$\begin{cases} u_1 = x_2^3 - 3x_1^2x_2 \\ u_2 = -x_1^3 + 3x_1x_2^2 \end{cases}. \tag{26}$$

This example is presented to show the accuracy and efficiency of the DiBFM with comparison to the conventional BEM. In the DiBFM, displacements and tractions are approximated by linear dual interpolation elements, while these variables are approximated by linear conforming elements in the BEM. Fig. 10 (b) shows the number of source nodes on each edge.

The relative errors of traction t_i on the whole boundary, and the CPU time spent in constructing and solving the system equations are listed in Table 1. In the table, *Err_t*$_1$ and *Err_t*$_2$ denote the relative errors of tractions t_1 and t_2, respectively. For greater clarity, the relative errors of traction t_1 are plotted in Fig. 11. Combined with the exact solution, the Von Mises stress along a curve *AB* is shown in Fig. 12. These numerical results are obtained by using 612 source nodes.

From Figs. 11 and 12, it clearly shows that the DiBFM can obtain more accurate results than the conventional BEM with the same number of source nodes. It is also concluded that our method is less sensitive to the mesh density than the conventional BEM. For example, the result relative error is only 0.5084% obtained by the DiBFM with 204 source nodes, while the relative error shoots up to 2.301% obtained by the conventional BEM with the same number of source nodes. The reasons for this are as follows: (i) the physical fields approximated by the linear dual interpolation elements are more accurate than that by the conventional linear elements; (ii) for the same number of source nodes, the application of the boundary conditions in the DiBFM is more accurate than that in the BEM, because the boundary conditions are imposed at source and virtual nodes in the DiBFM (see Eq. (24)), while these conditions are just imposed at source nodes in the BEM; and (iii) no geometric errors are introduced even in a coarse mesh, because the geometric data are calculated directly from the curves rather than from elements (see Section 2).

Fig. 13 shows the CPU time spent in constructing and solving the system equations. For the same level of accuracy, it is clear that the DiBFM requires less CPU time than the conventional BEM.

5.2. Thick-wall cylinder under internal pressure

The second example is a thick-walled cylinder subjected to a uniform pressure on the inner surface with $a = 100$, $b = 200$ and $p = 1$, where a and b indicate the inner and outer radius of the cylinder, and p is the uniform internal pressure. Due to the symmetry of the problem, only quarter of the structure is considered (see Fig. 14 (a)). Plane strain cases with Young's modulus $E = 2.5$ (in consistent units) and the Poisson's ratio $\nu = 0.3$ are assumed. The analytical solution for this problem is:

$$\begin{cases} \sigma_r = \frac{a^2p}{b^2-a^2}\left(1 - \frac{b^2}{r^2}\right) \\ \sigma_\theta = \frac{a^2p}{b^2-a^2}\left(1 + \frac{b^2}{r^2}\right) \\ u_r = \frac{(1+\nu)}{E}\frac{a^2p}{b^2-a^2}\left[(1-2\nu)r + \frac{b^2}{r}\right] \end{cases}. \tag{27}$$

In this example, the BIE is discretized by quadratic elements with different methods. Fig. 14 (b) shows the number of elements on each edge. Table 2 lists the relative errors of radial displacement u_r, radial

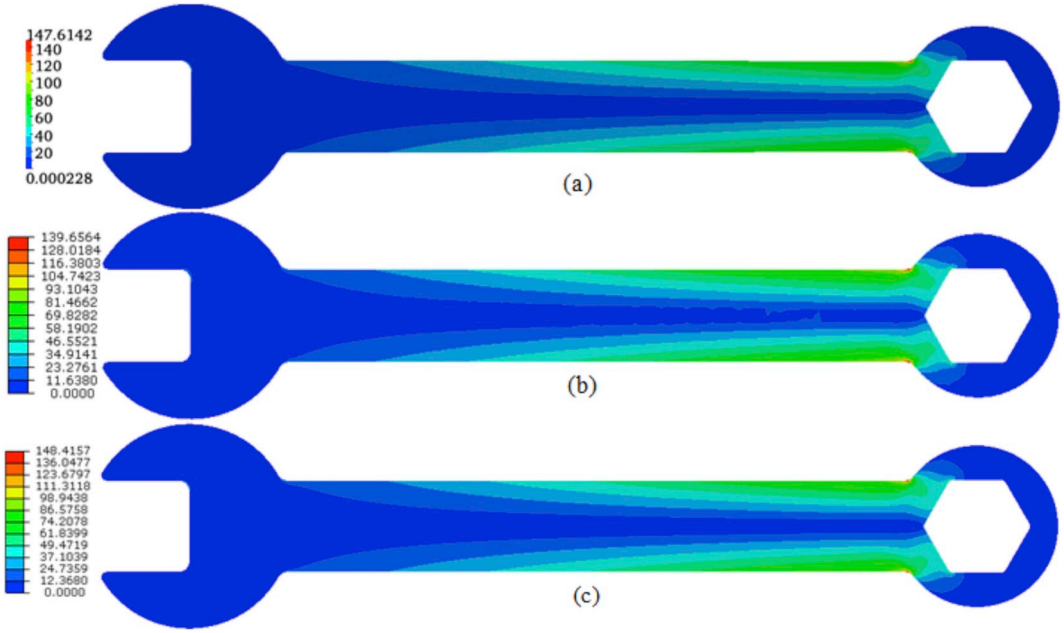

Fig. 20. Von Mises stress for combination wrench: (a) DiBFM with 348 source nodes, (b) FEM with 2049 source nodes, and (c) Reference Solution.

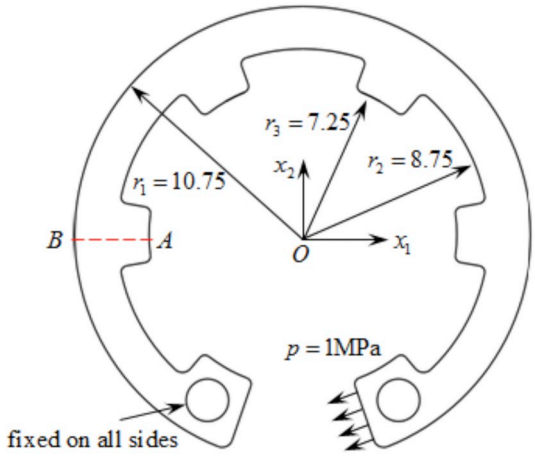

Fig. 21. Retaining ring: geometric model and boundary conditions.

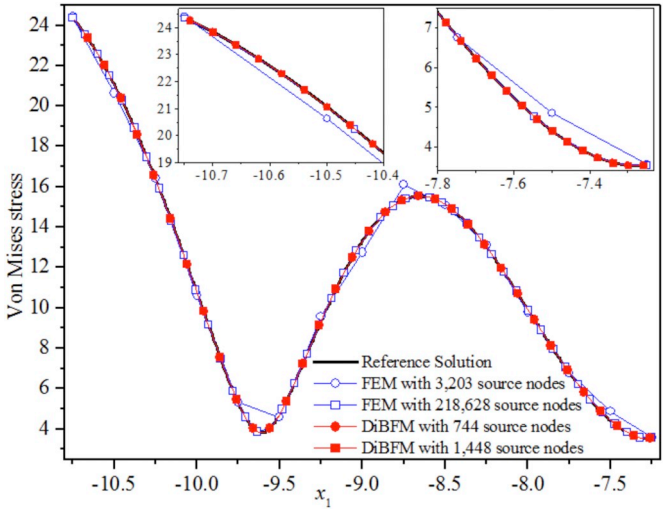

Fig. 22. Von Mises stress along the line *AB*.

Table 4
Numerical results for retaining ring.

DiBFM			FEM		
NE	*NS*	*Max_Mises* (MPa)	*NE*	*NS*	*Max_Mises* (MPa)
248	744	154.691	1450	3203	140.562
372	1116	154.880	27,610	56,605	153.953
496	1448	155.037	107,937	218,628	156.923
620	1860	154.995	423,925	853,340	156.942
744	2232	154.991	660,007	1,326,888	156.823
992	2976	154.999	2,628,209	5,270,170	156.430

stress σ_r and hoop stress σ_θ with different source nodes. In this table, symbols Err_u_r, Err_σ_r and Err_σ_θ denote the relative errors of u_r, σ_r and σ_θ, respectively. For greater clarity, the errors of σ_r are shown in Fig. 15. With 39 source nodes, the σ_r along an edge *AB* is plotted in Fig. 16. The CPU time spent in constructing and solving the system equations is illustrated in Fig. 17.

From Figs. 15–17, it can be seen that the DiBFM possesses much higher accuracy, convergence rates and computational efficiency than conventional BEM.

5.3. Combination wrench

To demonstrate the ability of DiBFM to handle arbitrary geometries, the problem of a combination wrench is analyzed under plane stress conditions with Young's modulus $E = 193$ GPa and Poisson's ratio $\nu = 0.27$. As shown in Fig. 18, a uniform pressure $p = 1$ MPa is imposed on edge *AB*, and the hexagon on the right end is fixed on all sides.

To validate the accuracy of our method, a comparison study between the DiBFM and the FEM has been made. In the DiBFM, the displacement and tractions are approximated by quadratic dual interpolation elements, while these variables are approximated by quadratic triangle elements in the FEM. Table 3 lists the numerical results obtained by the two methods with six sets of elements and source nodes. In Figs. 19 and 20, the numerical results obtained by FEM with 1,936,667 quadratic triangle elements and 3,881,639 nodes are denoted as a Reference Solution. Fig. 19 shows the Von Mises stresses along an edge *CD*, and Fig. 20 shows the contour plots of Von Mises stresses.

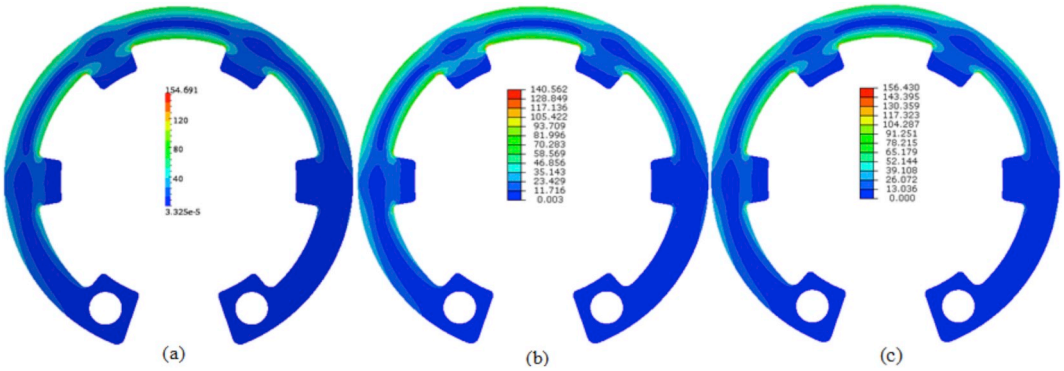

Fig. 23. Von Mises stress for combination wrench: (a) DiBFM with 744 source nodes, (b) FEM with 3203 source nodes, and (c) Reference Solution.

From Table 3 and Fig. 19, the comparison demonstrates that our method is efficient in calculating stresses. For the same number of source nodes, our method can lead to a highly accurate stress result.

5.4. Retaining ring

To demonstrate the ability of DiBFM to handle small sized features of a structure, the problem of a retaining ring was analyzed under plane stress case conditions with Young's modulus $E = 206$ GPa and Poisson's ratio $\nu = 0.3$. Fig. 21 shows the geometry and boundary conditions of the retaining ring.

The physical variables in this example are also approximated by quadratic elements as those in the third example. Numerical results obtained by the two methods with different source nodes are listed in Table 4. In Figs. 22 and 23, the results obtained by the FEM with 2,628,209 quadratic triangle elements and 5,270,170 nodes are denoted as a Reference Solution. Fig. 22 shows the Von Mises stress along a line AB, and Fig. 23 shows the contour plots of Von Mises stresses.

This example illustrates an important concept: the DiBFM has the potential to seamlessly interact with CAD software. The reason for this is that the geometry information of the computational model in our method is highly consistent with the B-rep data structure of the geometrical model in most CAD software.

6. Conclusions and discussions

A DiBFM has been proposed for solving 2D elasticity problems. This method is able to unify the conforming and nonconforming elements in BEM implementation. In the new method, displacements and tractions are approximated by the conforming elements, the same way as conforming BEM. BIEs are collocated at source nods only, the same way as nonconforming BEM. In consequence, the number of unknown nodal values is more than that of linear equations obtained by discretizing the BIE. To make the final system of linear equations solvable, additional constraint equations are needed to condense the degrees of freedom for all virtual nodes. These constraints are constructed by the MLS approximation. Thus, the size of the final coefficient matrix in the DiBFM is the same as that in the conventional BEM (see Eq. (24)), while the DiBFM can obtain higher computational accuracy.

The DiBFM is implemented based on B-rep data structure used in standard CAD software. Thus, it has the potential to seamlessly interact with CAD software. The geometry data in boundary integration and dual interpolation are directly calculated from curves (see Eq. (1)), thus no geometric errors are introduced. Besides, the MLS in the DiBFM is just used to assemble the coefficient matrices, rather than evaluate the shape functions at each Gaussian point in boundary integration. Meanwhile, in the process of MLS computation, the source nodes covered in the influence domain of a virtual node are obtained by directly searching the neighboring three layer elements (see Figs. 6–8). Thus, the efficiency of the MLS in our method is much higher than that of MLS in a pure mesh-free method.

The DiBFM has been verified by a number of numerical examples with real engineering background. It was observed that the solution was accurate for the displacements and stresses inside the domain and on the boundary. Compared with the BEM, it not only possesses higher accuracy, convergence rates and computational efficiency, but also is less sensitive to the mesh density. Extensions of the DiBFM to solving 3D problems will substantially simplify the mesh generation (see Fig. 2). This is an attractive advantage of our method. By coupling with the fast multipole method (Zhang et al., 2005, 2010; Zhang and Tanaka, 2008), it may be applied to perform large-scale computations for complicated structures. This is also ongoing.

Acknowledgements

This work was supported by National Natural Science Foundation of China under grant number 11772125 and 11472102.

References

Ang, W.T., Yun, B.I., 2011. A complex variable boundary element method for axisymmetric heat conduction in a nonhomogeneous solid. Appl. Math. Comput. 218 (5), 2225–2236.
Belytschko, T., Krongauz, Y., Organ, D., Fleming, M., Krysl, P., 1994. Element-free Galerkin methods. Int. J. Numer. Methods Eng. 37, 229–256.
Blázquez, A., París, F., 2011. Effect of numerical artificial corners appearing when using BEM on contact stresses. Eng. Anal. Bound. Elem. 35 (9), 1029–1037.
Carlone, P., Citarella, R., Sonne, M.R., Hattel, J.H., 2016. Multiple crack growth prediction in AA2024-T3 friction stir welded joints, including manufacturing effects. Int. J. Fatig. 90, 69–77.
Chen, J.T., Lee, Y.T., Lin, Y.J., 2010. Analysis of multiple-spheres radiation and scattering problems by using null-field integral equations. Appl. Acoust. 71, 690–700.
Citarella, R., Giannella, V., Lepore, M., Dhondt, G., 2018. Dual boundary element method and finite element method for mixed-mode crack propagation simulations in a cracked hollow shaft. Fatig. Fract. Eng. Mater. Struct. 41, 84–98.
Dong, C.Y., Yang, X., Pan, E., 2011. Analysis of cracked transversely isotropic and inhomogeneous solids by a special BIE formulation. Eng. Anal. Bound. Elem. 35 (2), 200–206.
Floreza, W.F., Powera, H., 2001. Comparison between continuous and discontinuous boundary elements in the multidomain dual reciprocity method for the solution of the two-dimensional Navier–Stokes equations. Eng. Anal. Bound. Elem. 25, 57–69.
Gao, X.W., Huang, S.Z., Cui, M., 2017. Element differential method for solving general heat conduction problems. Int. J. Heat Mass Tran. 115, 882–894.
Guiggiani, M., Krishnasamy, G., Rudolphi, T.J., Rizzo, F.J., 1992. A general algorithm for the numerical solution of hypersingular boundary integral equations. J. Appl. Mech. 59, 604–614.
Lancaster, P., Salkauskas, K., 1981. Surface generated by moving least squares methods. Math. Comput. 37, 141–158.
Lei, J., Zhang, C.Z., Bui, T.Q., 2015. Transient dynamic interface crack analysis in magnetoelectroelastic bi-materials by a time-domain BEM. Eur. J. Mech. Solid. 49, 146–157.
Li, X.L., Li, S.L., 2016. On the stability of the moving least squares approximation and the element-free Galerkin method. Comput. Math. Appl. 72 (6), 1515–1531.
Li, Y., Zhang, J.M., Xie, G.Z., 2014. Time-domain BEM analysis for three-dimensional elastodynamic problems with initial conditions. Comput. Model. Eng. Sci. 101 (3), 187–206.
Manolis, G.D., Banerjee, P.K., 1986. Conforming versus non-conforming boundary

elements in three-dimensional elastostatics. Internat. J. Numer. Methods Engrg 23, 1885–1904.
Mitra, A.K., Ingber, M.S., 1993. A multiple-node method to resolve the difficulties in the boundary integral equation method caused by corners and discontinuous boundary conditions. Internat. J. Numer. Methods Engrg 36, 1735–1746.
Parreira, P., 1988. On the accuracy of continuous and discontinuous boundary elements. Eng. Anal. 5 (4), 205–221.
Peake, M.J., Trevelyan, J., Coates, G., 2015. Extended isogeometric boundary element method (XIBEM) for three-dimensional medium-wave acoustic scattering problems. Comput. Methods Appl. Mech. Eng. 284, 762–780.
Rodríguez-Tembleque, L., Buroni, F.C., Abascal, R., 2011. 3D frictional contact of anisotropic solids using BEM. Eur. J. Mech. Solid. 30 (2), 95–104.
Schnack, E., Chen, H.B., 2001. A multi-variable non-singular BEM in 2D elasticity. Eur. J. Mech. Solid. 20 (4), 645–659.
Shen, L., Liu, Y.J., 2007. An adaptive fast multipole boundary element method for three-dimensional acoustic wave problems based on the Burton-Miller formulation. Comput. Mech. 40 (3), 461–472.
Shu, X.M., Zhang, J.M., Han, L., Dong, Y.Q., 2016. A surface-to-surface scheme for 3D contact problems by boundary face method. Eng. Anal. Bound. Elem. 70, 23–30.
Sladek, V., Sladek, J., 1992. Nonsingular formulation of BIE for plate bending problems. Eur. J. Mech. Solid. 11 (3), 335–348.
Tanaka, M., Chen, W., 2001. Dual reciprocity BEM applied to transient elastodynamic problems with differential quadrature method in time, Comput. Methods Appl. Mech. Engrg. 190 (18–19), 2331–2347.
Wang, H., Qin, Q.H., 2012. Boundary integral based graded element for elastic analysis of 2D functionally graded plates. Eur. J. Mech. Solid. 33, 12–23.
Wang, X.H., Zhang, J.M., Zhou, F.L., 2013. An adaptive fast multipole boundary face method with higher order elements for acoustic problems in three-dimension. Eng. Anal. Bound. Elem. 37, 114–152.
Wünsche, M., Sáez, A., García-Sánchez, F., 2012. Transient dynamic crack analysis in linear magnetoelectroelastic solids by a hypersingular time-domain BEM. Eur. J. Mech. Solid. 32, 118–130.
Xie, G.Z., Zhang, J.M., Cheng, H., 2014. A direct traction boundary integral equation method for three-dimension crack problems in infinite and finite domains. Comput. Mech. 53 (4), 575–586.
Zhang, J.M., Tanaka, M., 2008. Fast HdBNM for large-scale thermal analysis of CNT-reinforced composites. Comput. Mech. 41, 777–787.
Zhang, J.M., Tanaka, M., Endo, M., 2005. The hybrid boundary node method accelerated by fast multipole method for 3D potential problems. Int. J. Numer. Methods Eng. 63, 660–680.
Zhang, J.M., Qin, X.Y., Han, X., 2009. A boundary face method for potential problems in three dimensions. Int. J. Numer. Methods Eng. 80, 320–337.
Zhang, J.M., Zhuang, C., Qin, X.Y., 2010. FMM-accelerated hybrid boundary node method for multi-domain problems. Eng. Anal. Bound. Elem. 34, 433–439.
Zhang, Y.M., Gu, Y., Chen, J.T., 2011. Stress analysis for multilayered coating systems using semi-analytical BEM with geometric non-linearities. Comput. Mech. 47 (5), 493–504.
Zhang, J.M., Han, L., Dong, W.C. Lin, 2017a. A new implementation of BEM by an expanding element interpolation method. Eng. Anal. Bound. Elem. 78, 1–7.
Zhang, J.M., Lin, W.C., Dong, Y.Q., 2017b. A double-layer interpolation method for implementation of BEM analysis of problems in potential theory. Appl. Math. Model. 51, 250–269.
Zhang, J.M., Zhong, Y.D., Dong, Y.Q., 2018. Expanding element interpolation method for analysis of thin-walled structures. Eng. Anal. Bound. Elem. 86, 82–88.
Zhao, P., Qin, T.Y., Zhang, L.N., 2015. A regularized time-domain BIEM for transient elastodynamic crack analysis in piezoelectric solids. Eng. Anal. Bound. Elem. 56, 145–153.